# Simulation and Analysis of Human Micro-Dopplers in Through-Wall Environments

Shobha Sundar Ram, Craig Christianson, Youngwook Kim, and Hao Ling

*Abstract*—We present a simulation methodology for generating micro-Doppler radar signatures of humans moving behind walls. The method combines primitive-based modeling of humans with finite-difference time-domain (FDTD) simulation of walls. Realistic motions of humans are generated from computer animation data. The time-varying human radar cross section is simulated using the primitive-based prediction technique. The scattered returns of humans behind walls are then simulated by a hybrid of the human simulation model with the through-wall propagation data generated from FDTD. The resulting simulator is used to investigate the effects of walls of both homogeneous and inhomogeneous types on human micro-Dopplers. It is found that while through-wall propagation affects the magnitude response of the Doppler spectrogram in the form of attenuation and fading, it only introduces very minor distortions on the actual Doppler frequencies from the body parts. This is corroborated by measurement data collected using a Doppler radar, as well as by a point-scatterer analysis of refraction and multipath introduced by walls.

*Index Terms*—Finite-difference time-domain (FDTD) technique, humans, micro-Doppler, radar signatures, through-wall propagation.

## I. INTRODUCTION

IN RECENT years, there has been an increased interest in developing capabilities for detecting, tracking, and monitoring human activities behind walls in connection with law enforcement, surveillance, and search-and-rescue missions. Several different types of radio-frequency sensors, which have the capability of penetrating walls, have been developed for this purpose. These include ultrawideband (UWB) radars [1]–[5] and low-cost low-power Doppler radars [6]–[9]. Through-wall UWB radars can achieve a range resolution on the order of several centimeters. However, wall effects such as attenuation, refraction, and multipath introduce significant distortions in the radar signatures [1], [4]. Doppler radars facilitate the detection of moving targets such as humans by suppressing stationary background clutter. Also, the motions of different human limbs give rise to distinct features in the radar signature known as micro-Dopplers [10]–[12], which have been exploited for identification and classification of different human activities [13]–[16]. Even though Doppler radars have been operated in through-wall environments, the wall effects on human micro-Dopplers have not been adequately studied. One of the difficulties in addressing this problem is in developing a simulation model that can combine the scattering from dynamic human motions with through-wall wave propagation. The objectives of this paper are thus to address these deficiencies by: 1) developing a methodology for simulating human micro-Doppler signatures in complex through-wall environments and 2) analyzing the wall effects on human micro-Dopplers.

Human scattering has previously been modeled using computational electromagnetics techniques, such as the finite-difference time-domain (FDTD) technique [17] and high-frequency ray tracing (Xpatch) [18]. Both FDTD and Xpatch can yield very accurate radar signatures if a detailed model of a still human pose is available. However, the two techniques are computationally expensive and hence not very well suited for generating the radar signatures of dynamic human motions. In [12], van Dorp and Groen proposed a simple primitive-based prediction technique to model human gait. The different parts of the human body are modeled as primitive shapes such as ellipsoids and spheres whose radar cross sections (RCS) are well characterized. By using the time-varying phase centers of the different body parts of a walking human, one can readily compute the total RCS of the human. More recently, we have shown that the technique can be effectively combined with motion models derived from computer animation data to generate the Doppler radar signatures of dynamic objects such as humans and animals [19], [20]. Although the primitive-based technique does not model shadowing and multiple interactions between the different body parts, it is computationally fast and reasonably accurate when compared against the measured spectrograms.

For through-wall propagation simulation and phenomenology analysis, ray optical techniques have been used [18], [21]–[24]. While these methods succeed in modeling homogeneous wall structures such as concrete, adobe, and wood, the accuracy of such modeling for inhomogeneous walls made of bricks, reinforced concrete, or cinderblocks is more suspect [25]. Full-wave FDTD simulation provides more accuracy for such complex inhomogeneous structures at the expense of high computational cost.

In this paper, we propose the use of a hybrid model of primitive-based modeling of humans and FDTD simulations of walls to generate the radar signatures of humans behind walls. We substitute the free-space propagation factor between the radar and the human with the wall transfer function derived from FDTD modeling of the wall. This approach is detailed in Section II. The resulting simulations of the
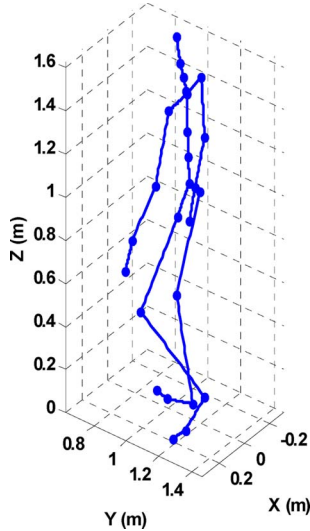
Fig. 1. Animation model of a walking human from Sony Computer Entertainment America.

micro-Doppler spectrograms of humans behind walls are presented in Section III. These simulation results enable us to investigate the effect of complex walls on human micro-Dopplers. They are validated with the measured data collected in line-of-sight and through-wall scenarios using a Doppler radar [8]. We further supplement the findings with an analytical study of the effect of wall refraction and multipath introduced by wall inhomogeneity on the Dopplers of a point target moving behind walls. The analyses are described in Section IV. In Section V, we study some additional complex through-wall scenarios. Finally, we present our conclusions in Section VI.

## II. HUMAN AND WALL SIMULATION METHODOLOGY

### A. Simulation of Human Scattering Using a Primitive-Based Prediction Model

We begin by summarizing the methodology for simulating the radar returns of realistic human motions derived from computer animation data that are generated from motion capture technology. This work was first presented by us in [19] and builds upon the primitive-based prediction technique of van Dorp and Groen [12], who simulated the radar returns from a walking human at a constant velocity based on the Thalmann model [26]. Typically, animation data describe two pieces of information. The first is the description of the initial pose of the human skeleton structure, and the second is the motion of the human. The center of gravity of the human lies at the hip joint. All $N$ bones in the skeleton are connected to the hip in a hierarchical manner through joints, as shown in Fig. 1. The motion of the hip is subject to 6 DOF: translation along the $X$-, $Y$-, and $Z$-axes, as well as Euler rotation about the three axes. All the other joints are subject to 3 DOF, namely, rotation about the three axes with respect to the initial pose. The time-varying 3-D position of every bone is computed by suitable matrix operations on the DOF data of the joints over time [19].

We assume that an electric-field incident on the moving human in free space is given by

$$E_i(r) = \frac{A}{r} e^{-j\frac{2\pi f_c}{c} r} \qquad (1)$$

where $f_c$ is the transmitter frequency, $A$ is a constant related to the gain of the antenna, and $r$ is the distance from the transmitter to the human. If we assume no interactions between the different human-body parts and a monostatic radar configuration, the scattered field from the human $[E_s(t)]$ can be generated by the complex sum of the RCS $(\sigma_b)$ of all $N$ body parts as follows:

$$E_s(t) = \frac{A}{\sqrt{4\pi}} \sum_{b=1}^{N} \sqrt{\sigma_b(t)} \frac{e^{-j\frac{2\pi f_c}{c} 2r_b(t)}}{r_b^2(t)}. \qquad (2)$$

In the aforementioned sum, the distance from the phase center of each part to the radar $r_b(t)$ is used to account for the different phase delays from the body parts. We model the human head as a sphere and the rest of the body parts associated with the other bones in the skeleton structure as ellipsoids, whose RCS is given in closed form by [27]

$$\sqrt{\sigma_b(t)} = \Gamma \left[ \frac{\frac{1}{4}\pi R_e^4 H_e^2}{\left(R_e^2 \sin^2 \theta_e(t) + \frac{1}{4}H_e^2 \cos^2 \theta_e(t)\right)^2} \right]^{1/2}. \qquad (3)$$

Here, $R_e$ and $H_e$ correspond to the radius and length of the ellipsoid with a circular cross section, respectively, and $\theta_e$ is the angle between the incident wave and the length axis of the ellipsoid. The phase center location $[r_b(t)]$ of an ellipsoid for a monostatic radar can be fairly well approximated by the point on the surface of the ellipsoid nearest to the radar. Because the human is not perfectly metallic, the relative permittivity of flesh is incorporated into the calculation of RCS via a reflection coefficient $\Gamma$. For $\Gamma$, we use the Fresnel reflection coefficient at normal incidence where the approximate conductivity and the dielectric constant of human body are 2 S/m and 80, respectively [28]. As a result of combining (2) and the motion information in the animation data, we can readily simulate the time-varying radar returns from the human in free space. The comparison of the simulation against measurement data taken in indoor line-of-sight environments of a human subject undergoing a variety of complex motions was previously reported in [19] and [32].

### B. Simulation of Wall Transfer Functions Using FDTD

Independent of the human simulation model described in the last section, we model the through-wall wave propagation phenomenology using an FDTD simulation [29]. We derive the wall transfer functions of two different walls: 1) a homogeneous concrete wall with a dielectric constant of seven and a conductivity value of 0.0498 S/m and 2) an inhomogeneous cinderblock wall with air holes, as shown in Fig. 2. To reduce the computational cost of the problem, the simulation is limited to two dimensions (i.e., assuming that the problem is $Z$ invariant). The area of the simulation is a 1.0 m $\times$ 1.5 m space ($X$: $-0.5$–$0.5$ m, $Y$: 0–1.5 m) bounded by a perfectly matched layer. A pulse source of 0.23-ns duration and vertically polarized in the $Z$-direction is placed at the position (0 m, 0.1 m), 0.2 m behind the wall that is 1 m wide in $X$ and 19.5 cm thick along $Y$. The simulator is run long enough to allow the wavefronts from the multiple bounces within the wall to reach the end of the simulation space. The time-domain electric field at every
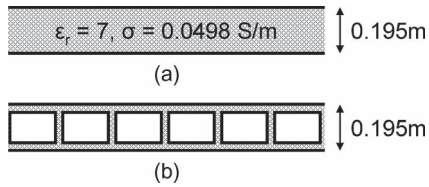
Fig. 2. Models of two different types of walls for FDTD simulations. (a) Homogeneous concrete wall and (b) inhomogeneous cinderblock wall that consists of concrete with air holes of dimensions of 15.25 cm in width and 13 cm in height.
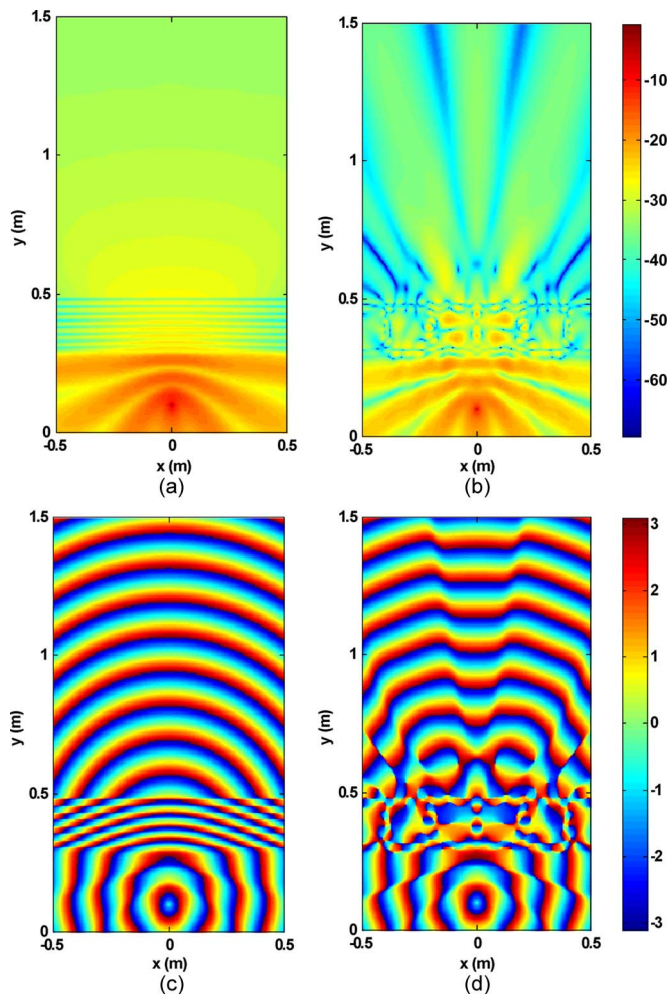


Fig. 3. Results from FDTD simulations. Magnitude response at 2.4 GHz for (a) homogeneous wall and (b) cinderblock wall. Phase response at 2.4 GHz for (c) homogeneous wall and (d) cinderblock wall.

point $\boldsymbol{\rho}$ in the FDTD grid space is then fast Fourier transformed to derive the wall-transmission response $[H_{\text{wall}}(f_c, \boldsymbol{\rho})]$ as a function of frequency and observation position. The magnitude responses for the two walls at 2.4 GHz are shown in Fig. 3(a) and (b). In Fig. 3(a), for the homogeneous-concrete-wall case, we observe the decay of the electric-field strength as the distance from the pulse source increases. The wall introduces an attenuation of 15 dB when compared to free space. Also, the magnitude response shows some directionality due to the angle-dependent transmission. Fig. 3(b) shows the magnitude response for the cinderblock wall. Again, the wall introduces significant attenuation on the transmitted signal. Moreover, the interior-wall inhomogeneity introduces multipath components

that interfere severely in certain regions (for instance, at azimuth angles of $55°$ and $83°$). Fig. 3(c) and (d) shows the phase responses for the two walls at 2.4 GHz. In Fig. 3(c), it is observed that, beyond the homogeneous wall ($Y$: 0.5–1.5 m), the transmitted wavefront remains a well-behaved circular wavefront throughout the simulation space. This is very similar to the phase response that would appear for a wave propagating in free space. However, when we consider the inhomogeneous-cinderblock-wall case in Fig. 3(d), the complex wavefronts from the multiple reverberations within the wall give rise to significant phase distortions, particularly near the wall.

### C. Hybrid Model of Human and Wall Simulation

Next, the wall transfer function derived from FDTD is combined with the human-scattering returns simulated from the animation models. If we ignore any higher order interactions between the human and the wall, this hybridization is quite simple. In principle, it is carried out by substituting the two-way free-space propagation factor between the radar and the phase center of each human-body primitive ($e^{-j(2\pi f_c/c)2r_b}/r_b^2$) by the square of the complex wall transfer function ($\{H_{\text{wall}}[f_c, \boldsymbol{r}_b]\}^2$). Although the operation appears straightforward, the following steps are followed to effectively hybridize the human and wall simulation models.

First, animation data are usually provided at a fixed frame rate between 60 and 240 Hz. Hence, the data must be suitably interpolated in time to prevent aliasing in the Doppler domain, particularly if a high carrier frequency is used because the Doppler frequency is directly proportional to the carrier. There are two possible interpolation methodologies that could be adopted. The first technique is independent interpolation of the coordinates of each joint of the human skeleton. However, the resultant interpolated data do not always correctly model the kinematics of rotating objects. A better way to interpolate the data, called spherical linear interpolation, has been widely adopted in the animation community [30]. It is based on describing the translation and Euler rotations of every joint using a four-coordinate system called a quaternion. Linear interpolation of data is carried out along the surface of the quaternion unit sphere. In our work, we use this latter approach to interpolate the animation data.

Next, the wall transfer functions from the 2-D FDTD simulation must be rescaled so as to correspond to the desired 3-D modeling. We note that the 2-D incident field due to a line source in free space is given by

$$E_i(\rho) = \frac{A'}{\sqrt{\rho}} e^{-j\frac{2\pi f_c}{c}\rho} \tag{4}$$

where $A'$ is a constant that is proportional to the current excitation used to drive the FDTD. Therefore, to translate the 2-D FDTD modeling into three dimensions, we rescale $H_{\text{wall}}[f_c, \boldsymbol{\rho}]$ from FDTD by the factor

$$C_{\text{2-D}\rightarrow\text{3-D}} = \left(\frac{\sqrt{\rho}}{r}\right)\left(\frac{1}{A'}\right) e^{-j\frac{2\pi f_c}{c}(r-p)}. \tag{5}$$

The rescaling is derived from free-space considerations but is carried out for the wall transfer function at every point $\boldsymbol{\rho}$. Third,
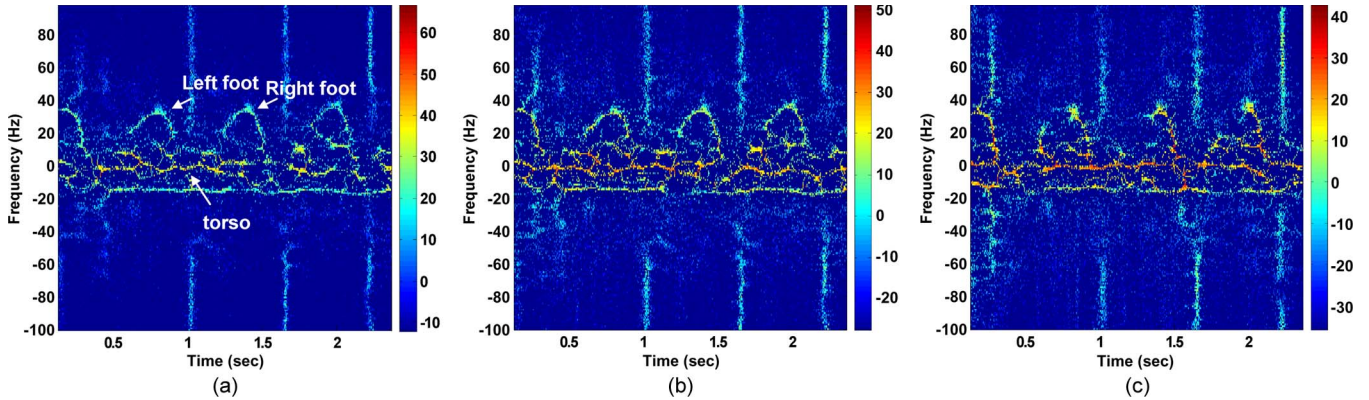
Fig. 4.    Results of simulations of human and wall. Reassigned Doppler spectrogram of a walking human at 2.4 GHz for (a) free space, (b) homogeneous wall, and (c) cinderblock wall.

it is also noted that the FDTD simulation generates the wall transfer coefficients only at the FDTD grid positions. Hence, a bilinear interpolation is carried out to compute $H_{\text{wall}}[f_c, \boldsymbol{\rho}_b]$ more accurately, where $\boldsymbol{\rho}_b(t)$ is the time-varying position coordinate of the bone primitive $[\boldsymbol{r}_b(t)]$ projected onto the 2-D FDTD simulation space.

Finally, the scattered returns of the human behind the wall are generated using

$$E_s(t) = \frac{A}{\sqrt{4\pi}} \sum_{b=1}^{N} \sqrt{\sigma_b(t)} \left\{ C_{\text{2-D}\to\text{3-D}} H_{\text{wall}} \left[ f_c, p_b(t) \right] \right\}^2. \quad (6)$$

To summarize, we have presented a hybrid methodology to combine the dynamic human signature predicted from a primitive model with the wall propagation effects computed from FDTD simulations.

## III.   RESULTS

### A.  Simulation Results

Using the methodology described in the previous section, we simulate the Doppler spectrograms of humans moving behind walls. Usually, the Doppler spectrogram $[\chi(t, f)]$ is generated by the application of the short-time Fourier transform (STFT) on the time-domain radar returns. Here, we instead opt to use the reassigned joint time–frequency transform to obtain an improved signal localization in the spectrogram [31]. We compute the instantaneous time $(t_{\text{inst}})$ and frequency $(f_{\text{inst}})$ from the derivatives of the phase $[\varphi(t, f)]$ of the STFT spectrogram as follows:

$$f_{\text{inst}} = \frac{1}{2\pi} \frac{\partial \varphi}{\partial t} \qquad t_{\text{inst}} = t - \frac{1}{2\pi} \frac{\partial \varphi}{\partial f}. \quad (7)$$

Then, we reassign $\chi(t, f)$ to $(t_{\text{inst}}, f_{\text{inst}})$ coordinates while ensuring that energy conservation is preserved.

A human-walking motion from Sony Computer Entertainment America's animation database is used. The animation data are provided at a fixed frame rate of 120 Hz. We first interpolate the data to 200 Hz to provide sufficient Doppler bandwidth to avoid aliasing effects. In order to ensure that the human motion is confined to the FDTD simulation space, we remove the translation movement of the human from the model

by fixing the human hip joint at the position (0 m, 1 m, 1 m). Fig. 4(a)–(c) shows the reassigned Doppler spectrograms that are generated when the human-motion model is combined with the FDTD results for free space and the two wall cases. The free-space result in Fig. 4(a) is checked first against the result obtained using (2), and the two spectrograms match very well. In Fig. 4(a), we observe that the Doppler of the torso is zero because of the zero translation motion of the human. The periodic features in the spectrogram arise due to the alternating motions of the left and right limbs. The feet returns have the highest Dopplers, followed by the lower legs and lower arms. The vertical streaks observed in the spectrogram are caused by short jerky movements in the computer-animated human. Fig. 4(b) shows the reassigned Doppler spectrogram that results when the human moves behind the homogeneous concrete wall. Except for a 15-dB attenuation introduced by the wall at 2.4 GHz, there appears very little distortion in the Doppler spectrogram when compared with that of free space. Next, we consider the inhomogeneous-cinderblock-wall case in Fig. 4(c). Some of the micro-Doppler features are now faded due to the severe attenuation introduced in some regions of space by the interfering multipaths due to the wall. However, the micro-Doppler frequencies appear to remain unchanged.

### B.  Measurement Results

The simulation results showed that the magnitude response of a wall was responsible for the key differences observed between the Doppler spectrograms of the free-space and through-wall cases. The actual micro-Doppler frequencies did not significantly change even in the presence of a complex inhomogeneous wall. To corroborate the simulation results, we collect measurement data using a 2.4-GHz Doppler radar [8]. First, we carry out the measurement under an indoor line-of-sight condition where the human subject walks toward the radar from 10 to 4 m and then turns around and walks away from the radar. Due to measurement noise, the reassigned spectrogram is not as effective in dealing with the measured data, and we revert to the standard STFT to display the data. The Doppler spectrogram is shown in Fig. 5(a). The spectrogram shows the same features observed previously in the simulated reassigned spectrogram in Fig. 4(a), such as the periodic features that arise due to the alternating motions of the limbs. In the measurement
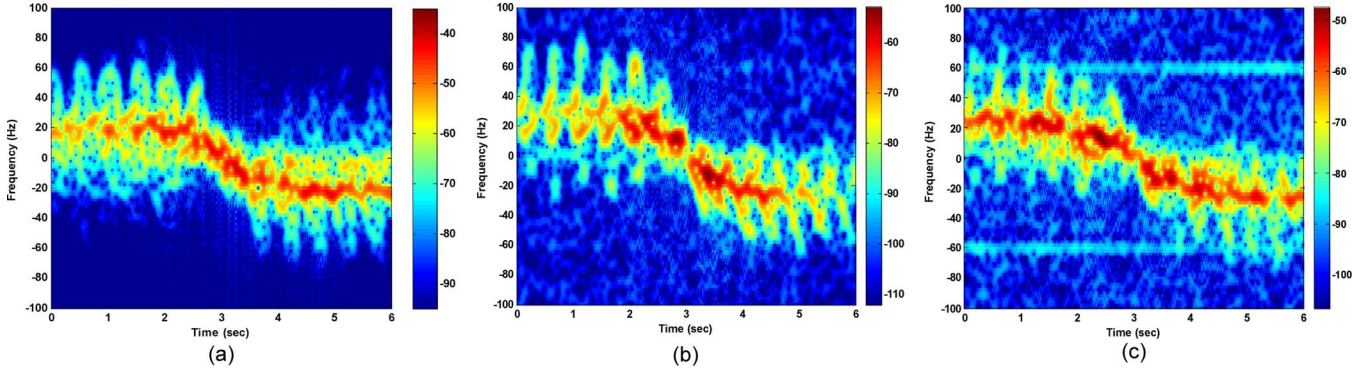
Fig. 5. Doppler spectrogram generated from measurement data collected using a Doppler radar testbed at 2.4 GHz for (a) indoor line of sight, (b) through exterior 15-inch brick wall, and (c) 12-inch cinderblock wall.
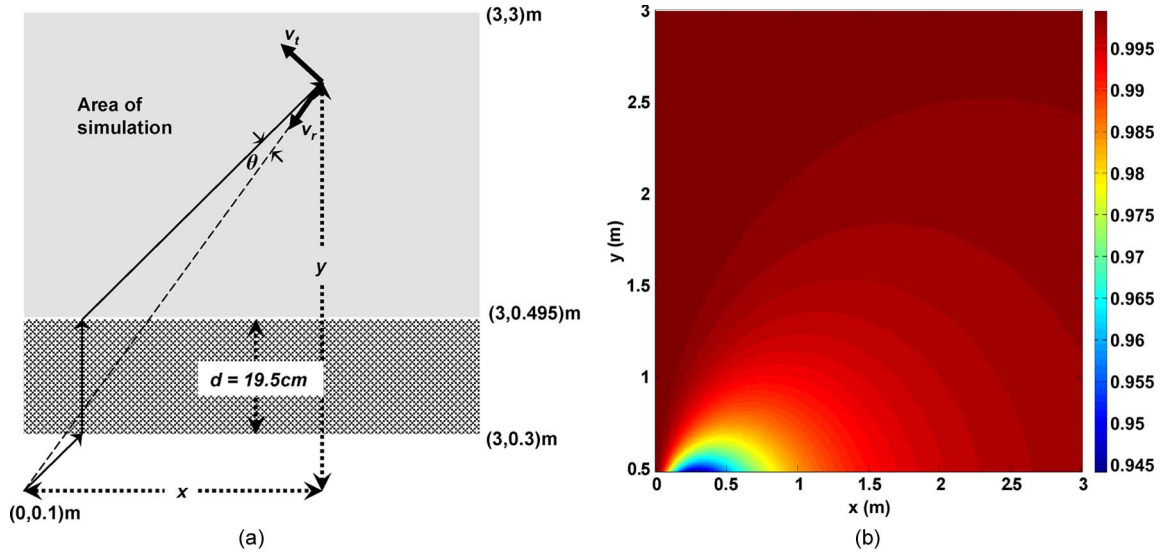


Fig. 6. Derivation of the effect of wall refraction on the Doppler of a point scatterer. (a) Simulation setup. (b) $\cos\theta$.

case though, the Doppler of the torso is not zero, unlike that in the simulation case where the translational motion was suppressed. Next, we repeat the measurement with the human subject behind an exterior brick wall of 15-inch thickness. From Fig. 5(b), we observe that the Doppler features are still preserved in this case in spite of the lowered signal strength caused by the wall attenuation. In the third case, we conduct the measurement with the subject behind a cinderblock wall of 12-inch thickness. The resulting Doppler spectrogram is shown in Fig. 5(c). In both of the through-wall cases, the subject walks from 6.8 to 1.8 m behind the wall, and the radar is placed 0.1 m in front of the wall. We observe from the measurement results that walls do not seem to alter the micro-Doppler frequencies of humans. To quantitatively substantiate this observation, we examine in more detail the effect of walls on the Doppler of a single point scatterer and a distributed target from an analysis viewpoint next.

## IV. QUANTITATIVE ANALYSIS OF WALL EFFECTS

A theoretical study of the effect of a wall on the Doppler return of a single point scatterer is carried out. First, we examine the effect of wave refraction caused by the wall. Next, we investigate the effect of multipaths introduced by more complex

walls using FDTD simulation. Finally, we analyze the effect of walls on the Doppler of a distributed target consisting of many point scatterers.

### A. Refraction

We assume a homogeneous wall of thickness $d$ and a monostatic radar setup, as shown in Fig. 6(a). The point scatterer, at a position $(x, y)$ with respect to the radar, moves with a velocity $(\nu_r)$ along the radial direction toward the radar. In the absence of a wall, the Doppler frequency of the point scatterer is $2f_c(\nu_r/c)$. When a wall of high permittivity is present, the wave gets refracted, as shown in the figure (where the angle of refraction approaches zero under the high-permittivity assumption). If we ignore the multiple bounces of the wave within the wall, the Doppler of the point scatterer is $2f_c(\nu_r/c)\cos\theta$, where $\theta$ is the angle between the direct and refracted waves. Thus, the difference in Dopplers in the two cases is directly proportional to $(\cos\theta - 1)$, where

$$\cos\theta = \cos\left[\tan^{-1}\left(\frac{x}{y-d}\right) - \tan^{-1}\left(\frac{x}{y}\right)\right]. \quad (8)$$

Assuming that the simulation space extends from $X$: 0–3 m and $Y$: 0.5–3 m and that the wall is 19.5 cm thick, the resulting
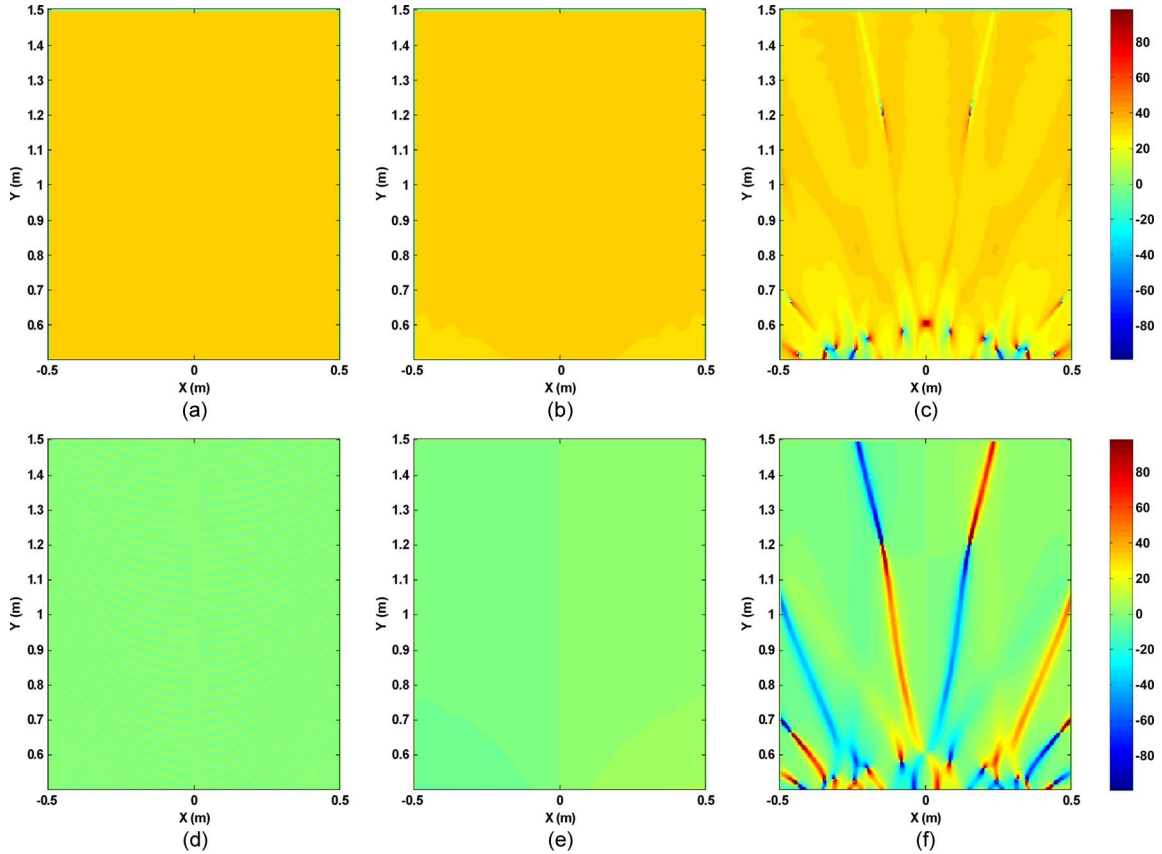
Fig. 7.   Doppler map for the radial path motion of a point scatterer at 2.4 GHz for (a) free space, (b) homogeneous wall, and (c) cinderblock wall. Doppler map for the tangential path motion of a point scatterer at 2.4 GHz for (d) free space, (e) homogeneous wall, and (f) cinderblock wall.

cosine plot is shown in Fig. 6(b). It is observed that, for most of the space, $\cos \theta$ is very close to one except for the small region in blue where the change is still less than 5.5%. If the point scatterer moves tangentially with respect to the radar with a velocity $\nu_t$, the Doppler of the point scatterer behind the wall becomes $2 f_c (\nu_t / c) \sin \theta$ instead of zero. Although the plot is not shown, $\sin \theta$ was found to be very close to zero for most of the simulation space (less than 0.06). The results of this paper illustrates that the Doppler frequency does not change significantly due to wall refraction.

*B. Multiple Bounces*

Next, we consider the effect of all the multiple bounces within a wall on the Doppler of a single point scatterer. We assume a point scatterer at a position $(x, y)$ in the FDTD grid space, moving with a radial velocity $(\nu_r)$ toward the radar. Then, the instantaneous Doppler at every point $(i, j)$ in the grid can be derived from the rate of change of phase $(\varphi)$ by the finite-difference formula

$$f_{i,j} = \frac{\nu_r}{\pi} \left[ \frac{\varphi_{i+1,j} - \varphi_{i+1,j}}{2 \Delta x} \cos \alpha_{i,j} + \frac{\varphi_{i,j+1} - \varphi_{i,j-1}}{2 \Delta y} \sin \alpha_{i,j} \right]$$

(9)

where $a_{i,j}$ is the angle between the velocity vector of the point scatterer and the $X$-axis. We assume purely radial motion for the point scatterer where the magnitude of the velocity is 2 m/s and the grid spacings are $\Delta x = \Delta y = 0.5$ cm. The

instantaneous Dopplers for the three FDTD simulation cases (free space and the two walls) are shown in Fig. 7(a)–(c). Ideally, for free space, the instantaneous Doppler at every point in the simulation space is 32 Hz at a frequency of 2.4 GHz. In Fig. 7(a)–(c), it is observed that the Doppler in most of the space is equal to 32 Hz. The small deviation (with an rms value of 0.1 Hz) that is detected in Fig. 7(a) is due to the FDTD numerical noise and finite-differencing error associated with (9). Fig. 7(b) shows the Doppler map for the homogeneous wall. A slightly higher deviation of 1 Hz is observed in the region that is very close to the wall. As seen earlier in Fig. 6(b), this effect is mostly a result of the significant wall refraction in this region. In the final case of the cinderblock wall in Fig. 7(c), there are some regions where the wall reverberation interferes destructively, thus resulting in very faded amplitudes. Because the phase is not well defined in these regions, the Doppler deviation from that of free space can be quite high. However, these regions manifest themselves in the spectrogram as amplitude fades. For most of the other spaces, the Doppler does not deviate from 32 Hz by more than 2 Hz.

Next, we assume that the point scatterer at position $(x, y)$ moves in a tangential path with respect to the radar. The Doppler is computed for every point in the grid space for each of the three cases using (9). This time, $\alpha$ is the angle between the tangential velocity vector $(\nu_t)$ and the $X$-axis. The results are shown in Fig. 7(d)–(f). The instantaneous Doppler for every point in the simulation space for free space is zero, as shown in Fig. 7(d) (numerical noise results in an rms deviation

of 0.1 Hz). However, higher Doppler deviations are observed in the through-wall cases. Wall refraction and multipath give rise to nonzero Dopplers in the homogeneous- and cinderblock-wall cases, as shown in Fig. 7(e) and (f). The rms Doppler deviation for the homogeneous-wall case is 1.3 Hz. In the cinderblock-wall case, some regions in Fig. 7(f) show very high Doppler deviation due to the ill-defined phase caused by amplitude fades. The rms Doppler error for the rest of the region is approximately 2 Hz. From this analysis, we find that the effect of walls on the Doppler frequencies of a single point scatterer is quite minor.

## C. Distributed Target

In addition to a single point scatterer, we examine the effect of walls on the Doppler of a moving distributed target. We consider a 1-m-long rod of negligible width modeled as a set of point scatterers that are spaced 0.5 cm apart. The midpoint of the rod is fixed at ($x = 0$ m, $y = 1$ m), and the rod undergoes angular rotation at a rate of $120°/s$ over a duration of 0.25 s (from $30°$ to $60°$ with respect to the $X$-axis), as shown in the inset of Fig. 8(a). The amplitude of the RCS of each point scatterer is set to unity. The time-domain radar returns from the rod are obtained at 2.4 GHz by the complex sum of the square of the wall transfer functions derived from FDTD simulations at the positions of each of the point scatterers. First, we consider the rod moving in free space. The radar is assumed to be located at (0 m, 0.1 m). The time-domain radar returns from the rod, which are sampled at 500 Hz, are Fourier transformed, and the result is shown in Fig. 8(a). The two dominant Doppler features observed in the Doppler spectrum arise from the two ends of the rod. The closer end of the rod moves toward the radar and gives rise to a strong positive Doppler return at 16 Hz, while the farther end gives rise to a weaker negative Doppler at $-12$ Hz. The Doppler frequencies from the two ends are not exactly equal and opposite because the radar is very close to the target. Next, we consider the rod rotating behind a homogeneous wall, as shown in the inset of Fig. 8(b). The Doppler spectrum from the rod is shown in Fig. 8(b). It is seen that although the homogeneous wall has attenuated the strength of the Doppler returns, there is no noticeable change in the frequencies of the Doppler peaks. Fig. 8(c) shows the Doppler spectrum of the rod rotating behind the cinderblock wall. Here, again, the Doppler peaks caused by the motion of the end points remain unchanged, even though the strengths have been attenuated. The sidelobe structure of the Doppler spectrum between the Doppler peaks is altered somewhat due to the phase distortion caused by the wall transmission experienced by the point scatterers along the rod. However, the frequencies of the Doppler peaks remain mostly unchanged. This finding is consistent with both the simulation and measurement data that we have reported earlier in Section III.

## V. FURTHER INVESTIGATIONS

Finally, we investigate some additional complex through-wall cases. First, we analyze the effect of walls on human Dopplers when the human is oblique to the radar. Next, we
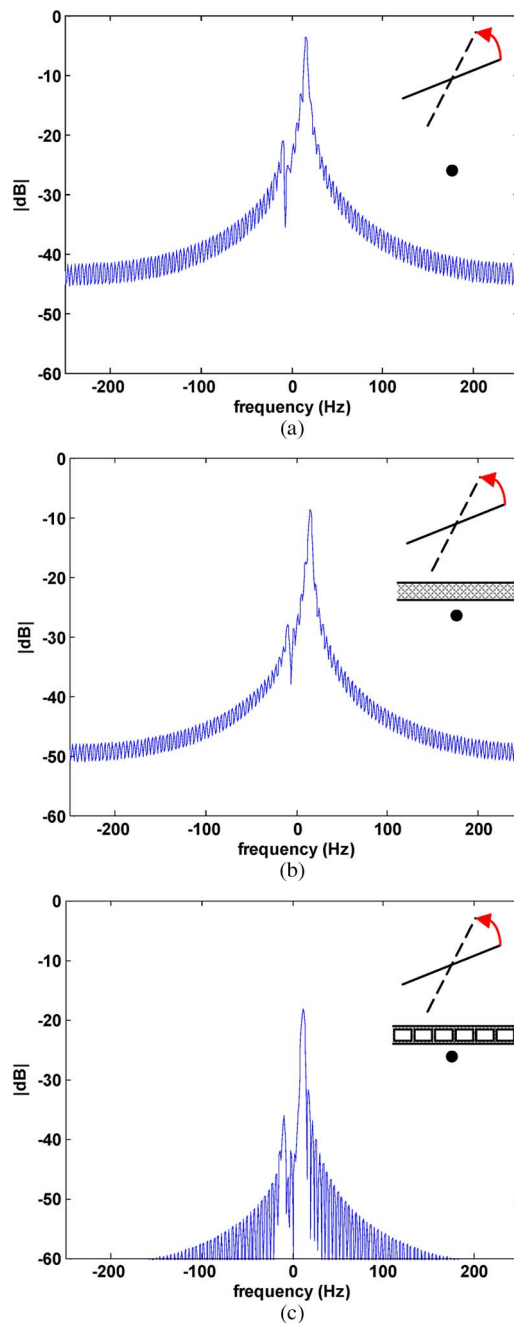


Fig. 8. Doppler returns of a 1-m rod rotating about (0 m, 1 m) in (a) free space, (b) behind the homogeneous wall, or (c) behind the cinderblock wall.

consider a case where the human is between two walls. This situation results in considerable interference between the waves bouncing off the two walls.

## A. Effect of Obliquely Incident Wave

In Section IV, we analyzed the effect of wall refraction on the Doppler of a moving point scatterer. The maximum Doppler deviation was observed when the point scatterer was oblique with respect to the radar. This deviation was caused by the significant wall refraction that is introduced at oblique angles. Therefore, we use our hybrid simulator to generate the Doppler spectrograms of a human walking at an oblique
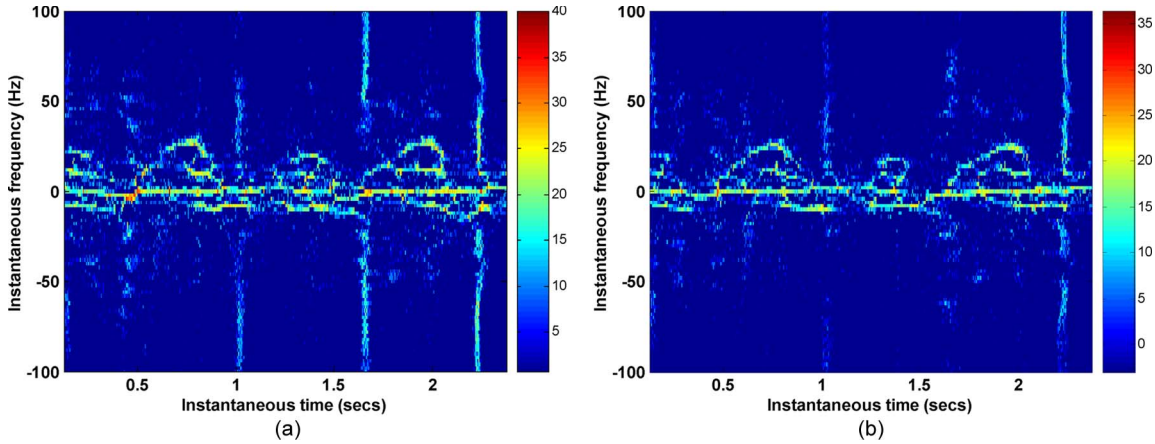
Fig. 9. Results of simulations of human and wall. Doppler spectrogram of a walking human (*human is oblique wrt radar*) at 2.4 GHz for (a) free space and (b) homogeneous concrete wall.
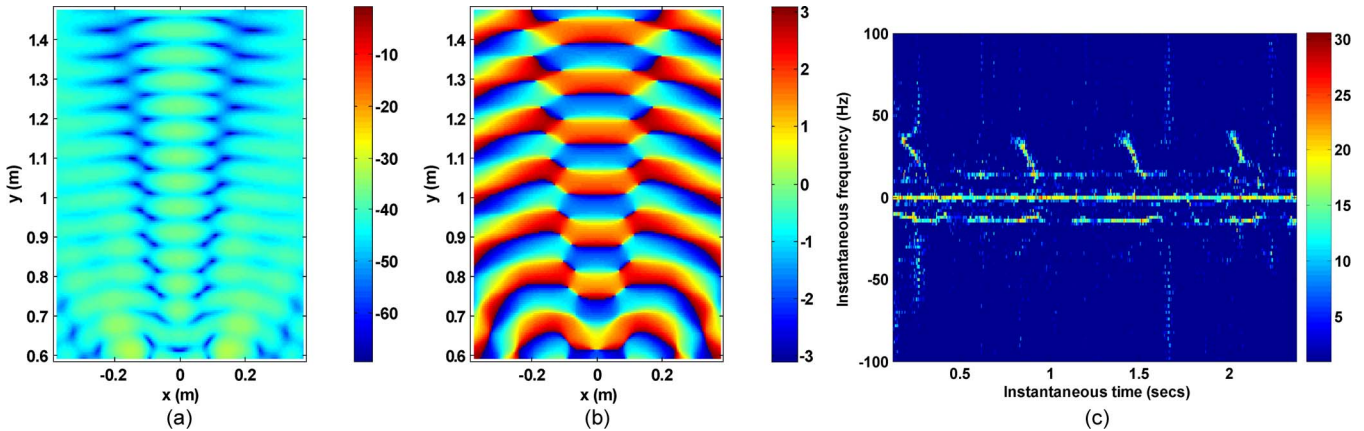


Fig. 10. Results of simulations of human between two cinderblock walls at 2.4 GHz. (a) Magnitude response. (b) Phase response. (c) Doppler spectrogram.

angle with respect to the wall. The transmission response is generated for the through-wall case for a simulation space that spans 1.5 m $\times$ 1.5 m ($X$: 0–1.5 m, $Y$: 0–1.5 m), assuming that the pulse source is located at (0 m, 0.1 m). The wall spans ($X$: 0–1.5 m, $Y$: 0.3–0.495 m). The translation motion of the human is suppressed again by fixing the human hip joint at (1 m, 1 m, 1 m). Fig. 9(a) and (b) shows the resulting Doppler spectrograms for the free-space and homogeneous-wall cases. The reassigned transform is used on the time-domain radar returns. The human motion is no longer radial with respect to the radar, and hence, the spectrogram shows lower Dopplers than Fig. 4(a). Also, the Dopplers from the left and right limbs are no longer equal because their positions are asymmetric with respect to the radar. When a homogeneous concrete wall is placed between the human and the radar, both wall refraction and multiple bounces are introduced. However, the Dopplers do not change significantly compared to the free-space case.

### B. Effect of Multiple Walls

Next, we consider the case when the human is situated between two walls. The FDTD simulation space spans 1.0 m $\times$ 2.0 m ($X$: −0.5–0.5 m, $Y$: 0–2 m). Two identical walls, which are 19.5 cm thick, span the $X$-axis and are located 0.2 and 1.67 m from the source (0 m, 0.1 m) along the $Y$-axis. The human animation model is constrained within the two walls by fixing the position of the hip joint at (0 m, 1.2 m, 1 m). The results of the cinderblock-wall case are shown in Fig. 10(a)–(c). Fig. 10(a) and (b) shows the magnitude and phase of the transmitted field at 2.4 GHz within the area where the human motion is constrained to occur. Due to reverberations between the two opposite walls, a standing-wave pattern is observed in the magnitude response. The phase response of the two-wall case in Fig. 10(b) is not considerably different from the single-wall case shown in Fig. 3(d). The resulting spectrogram is shown in Fig. 10(c). Compared to the results shown in Fig. 4(a), it is observed that the micro-Dopplers of some of the body parts are not visible due to the poor magnitude response. However, the phase distortions do not introduce significant deviations in the Dopplers.

### VI. CONCLUSION

We have developed a simulation methodology for generating the micro-Doppler radar signatures of humans moving behind walls. A primitive based prediction was applied to model the scattered returns from realistic human motions generated from computer animation data. We then combined the human modeling with independent wall-transmission data generated

using the FDTD technique. The hybrid was carried out by substituting the free-space propagation delay of each human part by the corresponding through-wall transfer function generated from FDTD. The resulting simulator was used to analyze the effects of different types of walls on human micro-Dopplers. It was found that while through-wall propagation affected the magnitude response of the Doppler spectrogram in the form of attenuation and fading, it only introduced very minor distortions on the actual Doppler frequencies from the body parts. This conclusion was supported by measurement data collected using a Doppler radar testbed and theoretical analyses of wall refraction and multipaths.

In this paper, only a 2-D FDTD simulation was used to account for the wall-transmission characteristics. A full 3-D FDTD analysis would provide a more accurate result at the expense of much higher computational resources. In fact, we have carried out the simulation of the transmission pattern of a reduced 3-D space (0.5 m × 0.75 m × 1 m) using CST Microwave Studio's transient solver. It was observed that the resulting phase responses for both wall cases did not significantly deviate from the 2-D results shown in this paper. Hence, the conclusions reached here will not be noticeably altered in the case of the full 3-D simulation. We also note that it is possible to use the same methodology introduced here to simulate the high-range-resolution profiles of humans behind walls from a wideband radar. Some preliminary results have been reported by us in [32]. It is interesting to point out that the degradation in the range returns caused by the wall can be quite severe. Therefore, significant processing will be needed to properly deconvolve the wall effects. In contrast, the Doppler information is little affected by through-wall propagation.

## REFERENCES

[1] S. Nag, H. Fluhler, and M. Barnes, "Preliminary interferometric images of moving targets using a time modulated using ultra wideband through-wall penetration radar," in *Proc. IEEE Radar Conf.*, May 2001, pp. 64–69.

[2] G. Franceschetti, J. Tatoian, D. Giri, and G. Gibbs, "Timed arrays and their application to impulse SAR for through-the-wall imaging," in *Proc. IEEE Antennas Propag. Soc. Int. Symp.*, Jun. 2004, vol. 3, pp. 3067–3070.

[3] F. Ahmad, Y. Zhang, and M. Amin, "Three-dimensional wideband beamforming for imaging through a single wall," *IEEE Geosci. Remote Sens. Lett.*, vol. 5, no. 2, pp. 176–179, Apr. 2008.

[4] M. Farwell, J. Ross, R. Luttrell, D. Cohen, W. Chin, and T. Dogaru, "Sense through the wall system development and design considerations," *J. Franklin Inst.*, vol. 345, no. 6, pp. 570–591, Sep. 2008.

[5] R. M. Narayanan, "Through-wall radar imaging using UWB noise waveforms," *J. Franklin Inst.*, vol. 345, no. 6, pp. 659–678, Sep. 2008.

[6] E. F. Greneker, "Radar flashlight for through the wall detection of humans," in *Proc. SPIE—Targets and Backgrounds: Characterization and Representation IV*, Apr. 1998, vol. 3375, pp. 280–285.

[7] E. F. Greneker, J. L. Geisheimer, D. S. Andreasen, O. D. Asbel, B. L. Stevens, and B. S. Mitchell, "Radar flashlight three years later: An update on developmental progress," in *Proc. IEEE Annu. Int. Carnahan Conf. Security Technol.*, Oct. 2000, pp. 257–259.

[8] A. Lin and H. Ling, "A Doppler and direction-of-arrival (DDOA) radar for multiple-mover sensing based on a two-element array," *IEEE Trans. Aerosp. Electron. Syst.*, vol. 43, no. 4, pp. 1496–1509, Oct. 2007.

[9] S. S. Ram and H. Ling, "Through wall tracking of humans using joint Doppler and array processing," *IEEE Geosci. Remote Sens. Lett.*, vol. 5, no. 3, pp. 537–541, Jul. 2008.

[10] J. L. Geisheimer, E. F. Greneker, and W. S. Marshall, "High-resolution Doppler model of the human gait," in *Proc. SPIE—Radar Sensor Technology and Data Visualization*, Jul. 2002, vol. 4744, pp. 8–18.

[11] V. C. Chen and H. Ling, *Time–Frequency Transforms for Radar Imaging and Signal Analysis*. Boston, MA: Artech House, 2002.

[12] P. van Dorp and F. C. A. Groen, "Human walking estimation with radar," *Proc. Inst. Elect. Eng.—Radar Sonar Navig.*, vol. 150, no. 5, pp. 356–365, Oct. 2003.

[13] M. Otero, "Application of a continuous wave radar for human gait recognition," in *Proc. SPIE—Signal Processing, Sensor Fusion, and Target Recognition XIV*, May 2005, vol. 5809, pp. 538–548.

[14] M. D. Anderson and R. L. Rogers, "Micro-Doppler analysis of multiple frequency continuous wave radar signatures," in *Proc. SPIE—Radar Sensor Technology XI*, May 2007, vol. 6547, p. 654 70A.

[15] T. Thayaparan, L. Stankovic, and I. Djurovic, "Micro-Doppler human signature detection and its application to gait recognition and indoor imaging," *J. Franklin Inst.*, vol. 345, no. 6, pp. 553–555, Mar. 2008.

[16] Y. Kim and H. Ling, "Human activity classification based on micro-Doppler signatures using a support vector machine," *IEEE Trans. Geosci. Remote Sens.*, vol. 47, no. 5, pp. 1328–1337, May 2009.

[17] T. Dogaru and C. Le, "SAR images of rooms and buildings based on FDTD computer models," *IEEE Trans. Geosci. Remote Sens.*, vol. 47, no. 5, pp. 1388–1401, May 2009.

[18] C. Le, T. Dogaru, L. Nguyen, and M. A. Ressler, "Ultrawideband (UWB) radar imaging of building interior: Measurements and predictions," *IEEE Trans. Geosci. Remote Sens.*, vol. 47, no. 5, pp. 1409–1420, May 2009.

[19] S. S. Ram and H. Ling, "Simulation of human micro-Dopplers using computer animation data," in *Proc. IEEE Radar Conf.*, May 2008, pp. 1–6.

[20] S. S. Ram and H. Ling, "Microdoppler signature simulation of computer animated human and animal motions," in *Proc. IEEE Antennas Propag. Soc. Int. Symp.*, Jul. 2008, pp. 1–4.

[21] T. B. Gibson and J. C. Jenn, "Prediction and measurement of wall insertion loss," *IEEE Trans. Antennas Propag.*, vol. 47, no. 1, pp. 55–57, Jan. 1999.

[22] M. Dehmollaian and K. Sarabandi, "Refocusing through building walls using synthetic aperture radar," *IEEE Trans. Geosci. Remote Sens.*, vol. 46, no. 6, pp. 1589–1599, Jun. 2008.

[23] R. J. Burkholder, P. C. Chang, R. J. Marhefka, and J. L. Volakis, "UTD ray tracing for building imaging studies," in *Proc. IEEE Antennas Propag. Soc. Int. Symp.*, Jul. 2008, pp. 1–4.

[24] R. J. Burkholder, R. J. Marhefka, and J. L. Volakis, "Radar imaging through cinder block walls and other periodic structures," in *Proc. IEEE Antennas Propag. Soc. Int. Symp.*, Jul. 2008, pp. 1–4.

[25] M. Dehmollaian and K. Sarabandi, "Hybrid FDTD and ray optics approximation for simulation of through-wall microwave imaging," in *Proc. IEEE Antennas Propag. Soc. Int. Symp.*, Jul. 2006, pp. 249–252.

[26] R. Boulic, M. N. Thalmann, and D. Thalmann, "A global human walking model with real-time kinematic personification," *Vis. Comput.*, vol. 6, no. 6, pp. 344–358, Nov. 1990.

[27] J. W. Crispin, Jr. and A. L. Maffett, "Radar cross-section estimation for simple shapes," *Proc. IEEE*, vol. 53, no. 8, pp. 833–848, Aug. 1965.

[28] C. Gabriel, S. Gabriel, and E. Corthout, "The dielectric properties of biological tissues. I. Literature survey," *Phys. Med. Biol.*, vol. 41, no. 11, pp. 2231–2249, Nov. 1996.

[29] C. Christianson, "Through-wall radar propagation study using finite difference time domain method," M.S. thesis, Univ. Texas, Austin, TX, May 2008.

[30] K. Shoemake, "Animating rotation with quaternion curves," *ACM SIGGRAPH Comput. Graph.*, vol. 19, no. 3, pp. 245–254, Jul. 1985.

[31] S. S. Ram and H. Ling, "Analysis of micro-Dopplers from human gait using reassigned joint time–frequency transform," *Electron. Lett.*, vol. 43, no. 23, pp. 1309–1311, Nov. 2007.

[32] S. S. Ram, C. Christianson, and H. Ling, "Simulation of high range-resolution profiles of humans behind walls," in *Proc. IEEE Radar Conf.*, May 2009, pp. 1–4.

Photographs and biographies of the authors not available at the time of publication.